ARCHIVIO ISTITUZIONALE
DELLA RICERCA

Alma Mater Studiorum Università di Bologna
Archivio istituzionale della ricerca

Coherent vibrational modes promote the ultrafast internal conversion and intersystem crossing in thiobases

This is the final peer-reviewed author's accepted manuscript (postprint) of the following publication:

Published Version:
Coherent vibrational modes promote the ultrafast internal conversion and intersystem crossing in thiobases / Teles-Ferreira D.C.; van Stokkum I.H.; Conti I.; Ganzer L.; Manzoni C.; Garavelli M.; Cerullo G.; Nenov A.; Borrego-Varillas R.; de Paula A.M.. - In: PHYSICAL CHEMISTRY CHEMICAL PHYSICS. - ISSN 1463-9076. - STAMPA. - 24:(2022), pp. 21750-21758. [10.1039/d2cp02073d]

Availability:
This version is available at: https://hdl.handle.net/11585/899366 since: 2022-11-03

Published:

DOI: http://doi.org/10.1039/d2cp02073d

Terms of use:

Some rights reserved. The terms and conditions for the reuse of this version of the manuscript are specified in the publishing policy. For all terms of use and more information see the publisher's website.

This item was downloaded from IRIS Università di Bologna (https://cris.unibo.it/).
When citing, please refer to the published version.

(Article begins on next page)

19 April 2024

Coherent vibrational modes promote the ultrafast internal conversion and intersystem crossing in thiobases

Received 00th January 20xx,
Accepted 00th January 20xx

DOI: 10.1039/x0xx00000x

Danielle Cristina Teles-Ferreira[a,b‡], Ivo HM van Stokkum[c‡], Irene Conti[e], Lucia Ganzer[d], Cristian Manzoni[d], Marco Garavelli[e], Giulio Cerullo [d,f] , Artur Nenov[e,*], Rocío Borrego-Varillas[d,*] and Ana Maria de Paula [a,*]

Thionated nucleobases are obtained by replacing oxygen with sulphur atoms in the canonical nucleobases. They absorb light efficiently in the near-ultraviolet, populating singlet states which undergo intersystem crossing to the triplet manifold on an ultrashort time scale with a high quantum yield . The primary mechanisms responsible for this ultrafast transition are still a matter of debate. Here we track both the electronic and vibrational ultrafast excited-state dynamics towards the triplet state for solvated 4-thiothymidine (4TT) and 4-thiouracil (4TU) with sub-30 fs broadband transient absorption spectroscopy in the ultraviolet. A global and target analysis allows us to simultaneously resolve the contributions of the different electronically and vibrationally excited states to the whole data set. Our experimental results, combined with state-of-the-art quantum mechanics/molecular mechanics simulations, support the population of a dark intermediate state and provide evidence that the relaxation to the triplet state is mediated by conical intersections promoted by vibrational coherences. An analysis of the coherent vibrational dynamics reveals that, despite sharing the same relaxation mechanism and similar chemical structures, 4TT and 4TU exhibit rather different geometrical deformations, characterized by the conservation of planarity in 4TU and its partial rupture in 4TT.

1 Introduction

Thiobase derivatives are obtained by replacing oxygen atoms with sulphur atoms in canonical nucleobases[1,2]. Although the structures of thio-derivatives are similar to those of the canonical bases, this substitution strongly modifies their absorption spectra and photophysical properties[3]. While the absorption spectra of canonical nucleobases peak in the UVC range, thiobases absorb predominantly in the UVB and UVA ranges[4]. In the canonical nucleobases, the presence of Conical Intersections (CIs)[5] allows for the ultrafast nonradiative re-population of the electronic ground state (GS) after UV photo-excitation, thereby promoting their remarkable photostability[5–8]. In contrast, the main deactivation pathway in thiobases is intersystem crossing (ISC) to a long-lived triplet state, rendering them poorly photostable[9–14]. The photogenerated triplet states in thio-derivatives are quenched by ambient oxygen, resulting in the production of highly reactive singlet oxygen which may lead to cell death. Thanks to their high triplet quantum yield, thioderivatives have proven useful for a variety of applications[10,15,16] such as photodynamic therapy[17,18], chemotherapy for the treatment of skin cancers[19] and superficial tumors[20] or as photolabels[21–23]. In this context, elucidating the photophysical mechanisms that determine the efficient and ultrafast triplet state population has become increasingly relevant[15,24–29] and key for the design of more efficient therapeutic agents.

In particular, in thiopyrimidines the relaxation pathways to the triplet manifold and the lifetime of the mediating states have been a matter of intense debate[30–35]. For the mono-substituted pyrimidines 4TU and 4TT, as well as the corresponding nucleosides and nucleotides[36], three pathways have been postulated in literature:

(i) $S_2(^1\pi\pi^*) \rightarrow S_1(^1n\pi^*) \rightarrow T_1(^3\pi\pi^*)$;
(ii) $S_2(^1\pi\pi^*) \rightarrow T_2(^3n\pi^*) \rightarrow T_1(^3\pi\pi^*)$;
(iii) $S_2(^1\pi\pi^*) \rightarrow T_1(^3\pi\pi^*)$.

We have recently demonstrated that in thiouracils the access to the triplet manifold depends on the degree of thionation and the excitation wavelength, leading to multiple ultrafast relaxation pathways[37,38]. In 4TU we identified pathway (i) as the dominant one in Phosphate-Buffered Saline (PBS) solution, while not ruling out the potential involvement of pathway (ii) as a secondary channel. The observed dynamics were modulated by an oscillatory pattern, a signature of a vibrational coherence established in the excited state (ES)[38]. Normal mode analysis showed that the underlying deformations preserve to a great extent the ring planarity.

For 4TT in aqueous solution Cui and Thiel identified all three pathways as equally feasible based on hybrid quantum mechanics/molecular mechanics (QM/MM) calculations[39]. Instead, Harada et al. postulated pathway (i) as the dominant one in acetonitrile solution based on transient absorption spectroscopy (TAS) experiments with 200 fs time resolution[40,41]. The dominant role of channel (i) was further corroborated by a joint experimental/theoretical study by Martínez-Fernández and co-workers on 4TT who observed only about 10% of the population undergoing pathway (ii)[42]. Furthermore, they revealed intriguing aspects of the molecular motion. In particular, while 4TT explores planar and twisted geometries in the $S_2(^1\pi\pi^*)$ state, the decay to the $S_1(^1n\pi^*)$ or the triplet manifold occurs predominantly from the twisted geometry.

Overall, while there is a general consensus that the deactivation mechanism involves internal conversion (IC)

[a] Departamento de Física, Universidade Federal de Minas Gerais, 31270-901 Belo Horizonte, MG (Brazil).
[b] Federal Institute of Minas Gerais-Ouro Preto, MG (Brazil).
[c] Department of Physics and Astronomy, Vrije Universiteit Amsterdam, De Boelelaan 1081, 1081HV Amsterdam (The Netherlands).
[d] IFN-CNR, Piazza Leonardo da Vinci 32, I-20133, Milano (Italy).
[e] Dipartimento di Chimica Industriale "Toso Montanari", Università degli Studi di Bologna, Viale del Risorgimento 4, 40136 Bologna (Italy)
[f] Dipartimento di Fisica, Politecnico di Milano, Piazza Leonardo da Vinci 32, I-20133, Milano (Italy).

†Electronic Supplementary Information (ESI) available. [4TU steady-state and transient absorption spectroscopy details. Critical Points and Conical Intersections Relative Energies (eV). Geometric parameters. Normal mode analysis. Cartesian Coordinates. DOAS and Target Analyses.] See DOI: 10.1039/x0xx00000x

‡ These authors contributed equally to this work.

through CIs and ISC, so far, the coherent vibrational dynamics promoting these processes has not been observed.

Here we present sub-30 fs TAS data for 4TT in PBS solution. The high temporal resolution of our experiment allows us to observe coherent oscillations superimposed on the ultrafast signatures of the IC and ISC processes. The data of 4TT are submitted to Damped Oscillation Associated Spectra (DOAS) and target analysis[43,44] to rationalize the vibrational and electronic spectral features for each wavelength simultaneously. A detailed assignment of the vibrational dynamics promoting the IC and ISC processes is supported by normal mode analysis, relying on state-specific normal modes obtained by explicitly considering effects of the environment through a hybrid QM/MM scheme. QM calculations are performed at the perturbatively corrected multi-configuration wave function level (the CASSCF/CASPT2 protocol, details in sec. 2.4). Our previous data for 4TU in Ref. [38] are revisited and subjected to the same analysis. We demonstrate that, while following similar relaxation mechanisms mediated by a dark state, 4TT and 4TU exhibit rather different geometrical deformations, thereby corroborating the previous findings by our group[38] and by Martínez-Fernández and co-workers[42]. The coherent vibrational dynamics revealed by the DOAS and rationalized by the normal mode analysis are associated with the system specific geometry changes in the course to the IC and ISC processes and allow to follow the ES deactivation pathways with an unprecedented level of detail.

2 Methods

2.1 Sample preparation

4TT was purchased from Carbosynth Ltd (UK) and used as received. The PBS solution at pH 7.4 in a concentration of 16 mM was prepared by dissolving 0.15 g of sodium dihydrogen phosphate and 0.27 g of sodium hydrogen phosphate in 200 mL of ultrapure water. The sample was dissolved in the PBS solution to obtain a concentration of 1.8 mM, giving an absorbance of 1 OD at the 330-nm central pump wavelength . The normalized steady-state absorption spectrum of 4TT and the pump-pulse spectrum are shown in Figure 1 (a). The same procedures were used for 4TU and its absorption spectrum can be found in the supplementary information (SI), Figure S1[38].

2.2 Pump-probe experimental setup

The experimental setup is described in detail in Ref.[45]. Briefly, 100-fs pulses from a Ti:Sapphire laser (central wavelength of 800 nm, 1 kHz repetition rate) drive a non-collinear optical parametric amplifier (NOPA), which generates sub-10-fs pulses with a bandwidth extending from 520 to 700 nm. Sub-20-fs pump pulses at 330 nm are obtained by sum frequency generation between a fraction of the fundamental beam and the visible pulses delivered by the NOPA[46]. The white-light continuum probe pulses (350-600 nm spectral coverage) are generated by focusing the fundamental beam in a CaF_2 plate. The pump and probe beams are non-collinearly focused on the sample in a flowing jet configuration. The setup instrumental response function (IRF) is estimated to be 30 fs[47]. The differential absorption (ΔA) of the probe beam is measured by a spectrometer as a function of the pump-probe delay.

2.3 Data analysis

Both 4TT (Figure 1(b)) and 4TU (Figure S1(b) and Ref.[38]) present a rich oscillatory pattern in the measured TAS map. For this reason, we employ a DOAS and target analysis[43,44], which allows us to simultaneously resolve the contributions of the different electronically and vibrationally excited states of the whole data set. The TAS map $\Delta A(t,\lambda)$, which is a function of the pump-probe delay (t) and the probe wavelength (λ), is fitted according to the model:

$$\Delta \boldsymbol{A}(\boldsymbol{t},\boldsymbol{\lambda}) = \sum_{l=1}^{N_{states}} \boldsymbol{c_l^S}(\boldsymbol{t'},\boldsymbol{\theta})\boldsymbol{SADS_l}(\lambda) + \sum_{n=1}^{N_{osc}} \boldsymbol{DOAS_n}(\boldsymbol{\lambda})\,\mathbf{cos}(\boldsymbol{\omega_n t'} - \boldsymbol{\varphi_n})\,\boldsymbol{e}^{-\gamma_n t'} \quad (1)$$

where the first term in the sum accounts for the electronic states evolution and the last one for the vibrational coherences, taking into account the Born-Oppenheimer approximation. In Equation (1) N_{states} represents the number of electronically excited states, c_l^S is the state population, N_{osc} is the number of vibrationally excited states, ω_n is the eigenfrequency, φ_n is the characteristic phase, and γ_n is the damping rate. $SADS_n(\lambda)$ are the Species Associated Difference Spectra, which give information of the spectral features of the electronically excited states for each species, while $DOAS_n(\lambda)$ contain the spectral information of the vibrational coherences for each mode. The analysis includes the parameters to fit the Coherent Artifact (CA) and the IRF as described in Ref.[43]. Further details can be found in the SI and Figures S2, S3 and S4.

2.3 Photoluminescence

In order to complement the understanding of the time-resolved data, we performed steady-state photoluminescence (PL) experiments for the samples at room temperature using a Cary Eclipse spectrophotometer with a lamp excitation at 330 nm. After preparation, the sample solution was pumped with N_2 to purge it from residual dissolved 0_2, which would lead to the formation of singlet oxygen. We subtract the contribution from the solvent in the data analyses.

2.4 Theoretical methods

Classical molecular mechanics simulations using the AMBER 12 suite[48,49] were employed to sample the conformational degrees of freedom of 4TT and 4TU dissolved in water. Thereby, the general AMBER force field (gaff) was used for the thionated nucleic acid 4TU and nucleoside 4TT, whereas the water molecules were described with the TIP3P force field[50]. The hydrogen-containing bonds were restrained by the SHAKE algorithm[51], while the water geometry was rigidized by the SETTLE scheme[52]. Nonbonding and electrostatic interactions were evaluated with a cut-off of 9 Å, using the particle mesh Ewald method for quantification of the long-range electrostatics. Thermalization of the systems was reached by heating of the preoptimized system to 300 K in 15 ps steps of 100 K. A production run at 300 K and 1 atm was carried out for 1 ns. Subsequently, a representative conformation with water molecules in a radius of 20 Å arranged in a spherical droplet was selected by means of a cluster analysis and was refined within a hybrid QM/MM scheme with electrostatic embedding. Thereby, the chromophore (uracil or thymine) was treated quantum-mechanically by means of second order perturbation theory (MP2), while the rest of the system was treated classically. The sugar moiety in 4TT as well as the nearest waters were allowed

to adapt during the geometry refinement. Starting from the relaxed GS geometry, critical points along the ES potential energy surface (PES) – S_2, S_1, T_2, T_1, CI(S_2/S_1) – were optimized at the XMS-*N*-CASPT2/SA-*N*-CASSCF(12,9) level of theory where $N = 3$ for singlet states (i.e. state averaging included GS, $^1n\pi^*$ and $^1\pi\pi^*$), $N = 2$ for triplet states (i.e. state averaging included $^3\pi\pi^*$ and $^3n\pi^*$) relying on numerical gradients and the ANO-L basis set with contractions S[4s3p2d1f], C,N,O [3s2p1d], H[2s1p][53]. The extended multi state (XMS) flavour of the CASPT2 method[54] was used for all geometry optimizations. The ionization-potential-electron affinity (IPEA) shift[55] was set to 0.0, and an imaginary shift[56] of 0.2 au was used throughout. The Cholesky decomposition was adopted to speed the evaluation of two-electron integrals. The QM/MM calculations were executed with the COBRAMM program, developed in our group interfacing the QM software OpenMolcas[57,58] with AMBER[59].

For each ES stationary point state-specific normal modes and frequencies verified its stationary character. The energetics of the singlet and triplet manifolds were refined by single point calculations with a larger ANO-L contraction S[5s4p2d1f], C,N,O [4s3p2d1f], H[3s2p1d]. Finally, the manifold of higher lying ES that give rise to photoinduced absorption features in the spectra were computed with a state averaging over 30 states with the multi state (MS) flavour of CASPT2[60], thus covering the energy range of approximately 8 eV above the GS. Transition dipole moments and spin-orbit couplings were evaluated with the RASSI module of OpenMolcas. For consistency reasons stationary points along the ES PES of 4TU, published previously,[40] were re-optimized.

Normal mode analysis projects the geometrical differences on the state-specific normal modes, thereby allowing to identify the "active" modes in each electronic state, i.e. the deformations which connect the structures along the relaxation path from the Franck Condon (FC) point to the T_1 minimum (for further details see sec. 5 of the SI). Specifically, S_2 normal modes were used to project geometrical deformations from the FC to the S_2 minimum, as well as from the S_2 minimum to the CI(S_2/S_1). S_1 normal modes were used to project the deformations in the S_1 state from the CI towards the corresponding minimum. Finally, T_1 normal modes were used to study the geometrical deformations from the S_1 minimum (where S_1 and T_1 are nearly degenerate and exhibit a pronounced spin-orbit coupling) to the T_1 minimum. Comparative analysis between the modes allows for identifying modes which are state-specific and those that contribute to the vibrational dynamics in all states. The normal mode analysis with state specific normal modes allows us to critically re-evaluate and extend the analysis performed by us previously based solely on the GS normal modes[40].

3 Results and discussion

Figure 1 summarizes the experimental TAS results for 4TT dissolved in a PBS solution at pH 7.4. Panel a shows the 4TT normalized steady-state absorption (black curve), pump pulse spectrum (red curve) and the PL spectrum (blue curve). The PL spectrum shows two broad bands peaking at 400 nm and 545 nm. The first one is related to the fluorescence from S_2, whereas the second one is assigned to the phosphorescence from the triplet state[2].

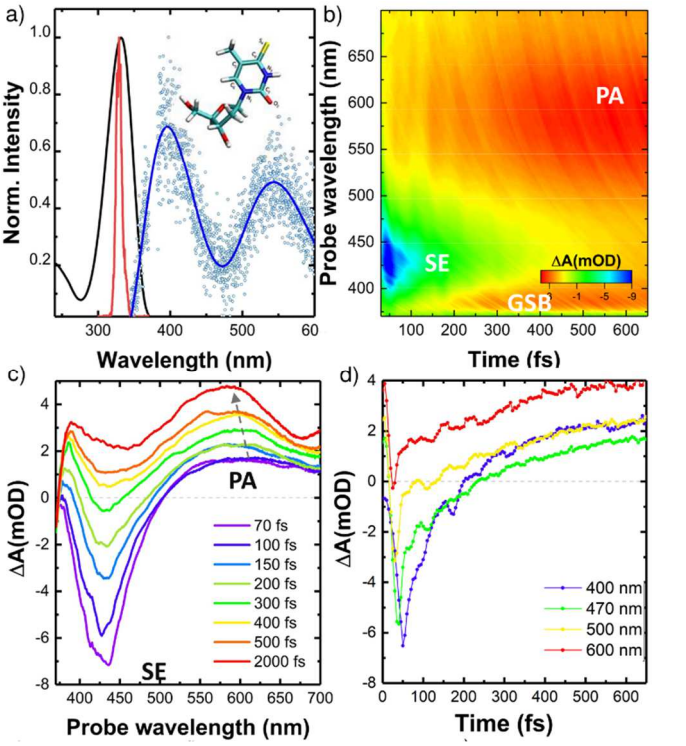

Figure 1 - a) 4TT normalized optical absorption spectrum (black curve), normalized pump pulse spectrum (red curve), and normalized PL spectrum (blue curve is the fit and blue dots are the data) obtained pumping the sample at 330 nm. b) 4TT ΔA map as a function of delay and probe wavelength. c) 4TT ΔA spectra at selected time delays. d) 4TT ΔA dynamics at selected probe wavelengths.

The ΔA map as a function of time delay and probe wavelength is displayed in Figure 1(b). Figures 1(c) and 1(d) show cuts of the ΔA map at selected time delays and wavelengths, respectively. At early times three signals are observed: the Ground State Bleaching (GSB) below 370 nm, a Stimulated Emission (SE) band peaking at about 420 nm and decaying on a sub-ps time scale and a Photoinduced Absorption (PA) signal above 500 nm rising after a few hundred fs. The presence of a PL peak at ≈400 nm confirms the assignment of the negative peak at 420 nm to SE from the bright $S_2(^1\pi\pi^*)$ state. The PA band has been observed in previous studies with a lower time resolution of 200 fs[18] and has been assigned to a triplet-triplet absorption, thus providing a fingerprint of the ISC process. Simultaneously with the sub-ps rise of the triplet PA we observe a vibrational cooling documented by the blue-shift of this band (Figure 1(c) , dashed arrow)[61]. The calculated values for the emission from the minimum on the $S_2(^1\pi\pi^*)$ state termed $Min_{TT}S_2$ (411 nm, red curve in Figure 2(a)) and for the PA from the minimum on the $T_1(^3\pi\pi^*)$ termed $Min_{TT}T_1$ (633 nm, orange curve in Figure 2(a)) corroborate these assignments. All these signals are also observed for 4TU[38]. The ΔA map of 4TU, which is qualitatively very similar to that of 4TT, is described in detail in ref.[38] and presented in Figure S1.

The ΔA dynamics at different wavelengths for 4TT (Figure 1 (d)) and 4TU (Figure S1 (d)), show a modulation by an oscillatory pattern from vibrational coherences impulsively excited by the sub-20-fs pump pulse.

The DOAS and target analysis allowed us to disentangle these oscillatory features from the electronic contributions. The target analysis results are presented in Figure 3. Panels (a)-(e)

present the analysis results for 4TT and panels (f)-(j) the ones for 4TU. Details of the kinetic schemes used are shown in Figure S2 of the SI.

Figure 3 presents the population dynamics (a), the oscillations (b) and the SADS (Species Associated Difference Spectra) (c) for 4TT. The black SADS is associated with the SE/PA spectrum of the bright $S_2(^1\pi\pi^*)$ state. As discussed above, the negative band is due to SE whereas the positive band above 500 nm arises due to characteristic PA from the $S_2(^1\pi\pi^*)$ state, in agreement with the calculated PA bands at 466 nm, 549 nm and 892 nm from $Min_{TT}S_2$ (Figure 2 (a)). We note that the 466 nm PA (transient dipole moment of 1.35 a.u.) is to a large degree covered by the stronger SE (transient dipole moment of 2.50 a.u.) and only its tail is visible through its contribution to the positive band above 500 nm. According to the target analysis, a bifurcation of the S_2 wave packet occurs with a time constant of 67 fs. Thereby, approximately half of the population (precisely 56%) undergoes an ultrafast IC to the $S_1(^1n\pi^*)$ state, facilitated by the relatively small barrier to the CI seam of ca. 20 meV (Figure 2(a)). The rest of the $S_2(^1\pi\pi^*)$ population relaxes in the $^1\pi\pi^*$ state, a process associated with a red-shift of SE due to the spreading of wave packet on the PES. This is reflected in the SADS (green line in Figure 3(c)) characterized by a SE feature with a weak contribution in the 500-700 nm range. The $S_2(^1\pi\pi^*)$ state is completely depleted with a 168 fs time constant. The existence of a longer living fraction in the $S_2(^1\pi\pi^*)$ state (44%) allows for ISC to the triplet manifold to kick in. In fact, the target analysis reveals that about 10% of the $S_2(^1\pi\pi^*)$ population undergoes direct ISC. In agreement with El-Sayed's rules we find a comparably strong spin-orbit coupling of 135 cm^{-1} between $S_2(^1\pi\pi^*)$ and $T_2(^3n\pi^*)$. As a consequence, the triplet state population (magenta line in Figure 3(a)) begins to accumulate already on the sub-100 fs time scale despite the fact that the $S_1(^1n\pi^*)$ state, the main gateway to the triplet manifold, has a lifetime of 445 fs.

The long $S_1(^1n\pi^*)$ lifetime allows for the accumulation of nearly 60% of the population in the first few hundred femtoseconds (red line in Figure 3(a)). Interestingly, according to the calculations, at $Min_{TT}S_1$ the $S_1(^1n\pi^*)$ state is not completely dark in the probed spectral window and is expected to exhibit weak PA signals around 370 nm and 570 nm, accompanied by a SE at 515 nm, almost two orders of magnitude weaker than the SE from the S_2 state (Figure 2(a) and Figure 4). The SADS of the $S_1(^1n\pi^*)$ state (red curve in Figure 3(c)) agrees well with the calculations, exhibiting positive contributions at 390 nm and above 450 nm. The $S_1(^1n\pi^*)$ state is depleted through ISC to the triplet manifold with a 445 fs time constant. Notably, we calculated spin-orbit couplings of similar magnitude (approximately 100 cm^{-1}) to both T_1 and T_2 which have mixed $n\pi^*/\pi\pi^*$ character at $Min_{TT}S_1$. The triplet manifold exhibits a SADS (magenta line in Figure 3(c)) with PA signatures throughout the entire probing window, peaking at its lower edge around 380 nm and a broad band at around 600 nm, in agreement with the calculated PA signatures at 349 nm and 633 nm ($Min_{TT}T_1$ in Figure 2 (a)). Cooling in the T_1 state is found to occur with a time constant of 1.76 ps leading to the formation

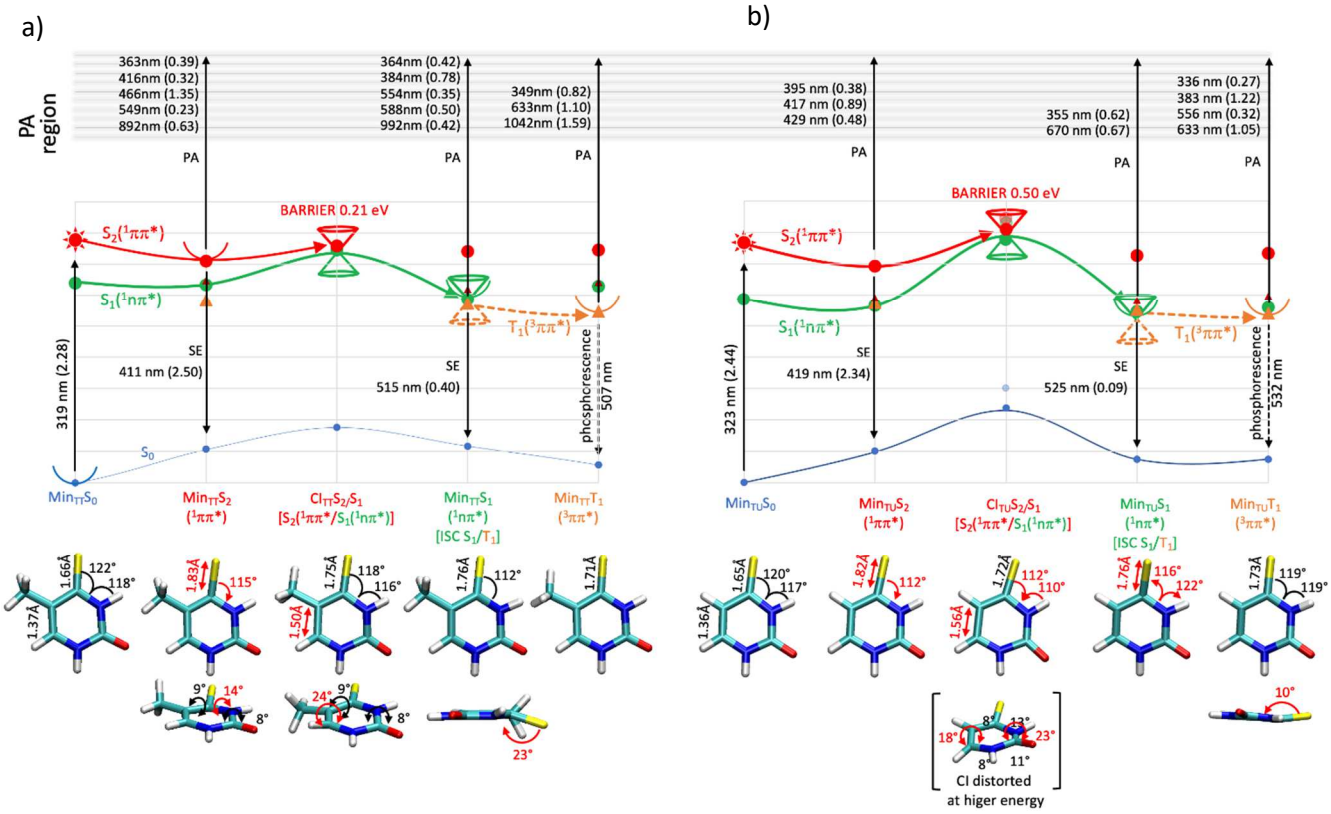

Figure 2 - Photoinduced internal conversion mechanism in 4TT (a) and 4TU (b) in aqueous solution together with major geometrical deformations along the relaxation path. The pump pulse populates the $S_2(\pi\pi^*)$ as indicated by the vertical black arrow from the GS minima. Relaxation into the lowest triplet state occurs along the $S_2(^1\pi\pi^*$, red) → $S_1(^1n\pi^*$, green) → $T_1(^3\pi\pi^*$, brown) pathway mediated by a conical intersection CI(S_2/S_1) and by an efficient intersystem crossing ISC(S_1/T_1). Transition wavelength and transition dipole moment (TDM, in brackets) of the characteristic stimulated emission and absorption features from the S_2, S_1 and T_1 minima are displayed.

of a long-lived component (blue SADS in Figure 3(c)), which closely resembles that of the unrelaxed T_1 species.

In a nutshell, the target analysis of 4TT shows a mismatch between the time scales of the $S_2(^1\pi\pi^*)$ depletion, described by a bi-exponential profile with time constants of 67 fs and 168 fs, and of the triplet formation, exhibiting a linear rise in the first few hundred femtoseconds (Figure 3(a)), thus providing experimental evidence for the $S_2(^1\pi\pi^*) \rightarrow S_1(^1n\pi^*) \rightarrow T_1(^3\pi\pi^*)$ mechanism (see Figure 4). The short $S_2(^1\pi\pi^*)$ lifetime matches well with the theoretical prediction by Cao et al., who assigned a transition from the excited singlet state $S_2(^1\pi\pi^*)$ to the dark singlet state $S_1(^1n\pi^*)$ within 100 fs for 4TT in water[62]. Finally, the estimate of 10% of the population undergoing pathway (ii) is in agreement with the theoretical results of Martínez-Fernández and co-workers[42].

A target analyses was also performed on the 4TU data (previously reported in ref.[38]). The results are shown in Figure 3 (f)-(j). As in 4TT $S_2(^1\pi\pi^*)$ is depleted bi-exponentially, with 124 fs and 353 fs time constants, thus notably more slowly compared to 4TT, which correlates well with the higher barrier to the CI seam of 50 meV (Figure 2(b)). In contrast to 4TT, we do not observe a red-shift of the SE which is attributed to the fact that 4TU preserves planarity during the evolution on $S_2(^1\pi\pi^*)$ (see next paragraph for discussion on the geometrical deformations along the relaxation profiles). Therefore, the SADS of the shorter and longer living fractions in the $S_2(^1\pi\pi^*)$ state are identical (black line in Figure 3(h)). The slower $S_2(^1\pi\pi^*)$ depletion facilitates an efficient ISC and as a consequence, despite $S_2(^1\pi\pi^*) \rightarrow S_1(^1n\pi^*) \rightarrow T_1(^3\pi\pi^*)$ remaining the dominant pathway, a significant fraction of the population (approximately 40%) is found to undergo pathway (ii). Due to the efficient ISC the mismatch between the $S_2(^1\pi\pi^*)$ depletion and triplet rise is not as pronounced as in 4TT. Moreover, the population in the $S_1(^1n\pi^*)$ state rises to just 40% in the first 300 fs. The SADS of the $S_1(^1n\pi^*)$ and $T_1(^3\pi\pi^*)$ show PA features in remarkable agreement with the computed values (for details see the assignment in Figure S5).

Despite sharing a similar molecular structure and identical decay mechanism, the geometrical deformations in 4TT and 4TU along pathway (i) from the FC point to the triplet manifold are, somewhat surprisingly, dissimilar. For both systems the initial relaxation from the FC point towards the $S_2(^1\pi\pi^*)$ minima ($Min_{TT}S_2$ and $Min_{TU}S_2$, respectively) is mainly associated with C_4-S_4 elongation (see Tables S3 and S4 in the SI). However, while in 4TU the system remains planar, we observe a slight pyramidalization of C_4 in 4TT (Figure 2). The access to the CI is associated with a pronounced elongation of the C_5-C_6 bond. Some other bonds exhibit considerable changes that are very similar in both systems. The main difference between the two systems is that in 4TU the CI is reached by in-plane bending of the sulphur S_4 and the adjacent hydrogen H(-N_3) whereas in 4TT the CI is reached by H_3C-C_5-C_6-H out-of-plane deformation by ca. 24° (Figure 2). It should be noted that the planarity conserving and breaking paths are accessible in both 4TU and 4TT, but which one is energetically preferred (i.e. associated with a lower barrier) is seemingly decided by the small changes of the PES topology induced by the replacement of a hydrogen with a methyl group. The relaxation from the CI to the $S_1(^1n\pi^*)$

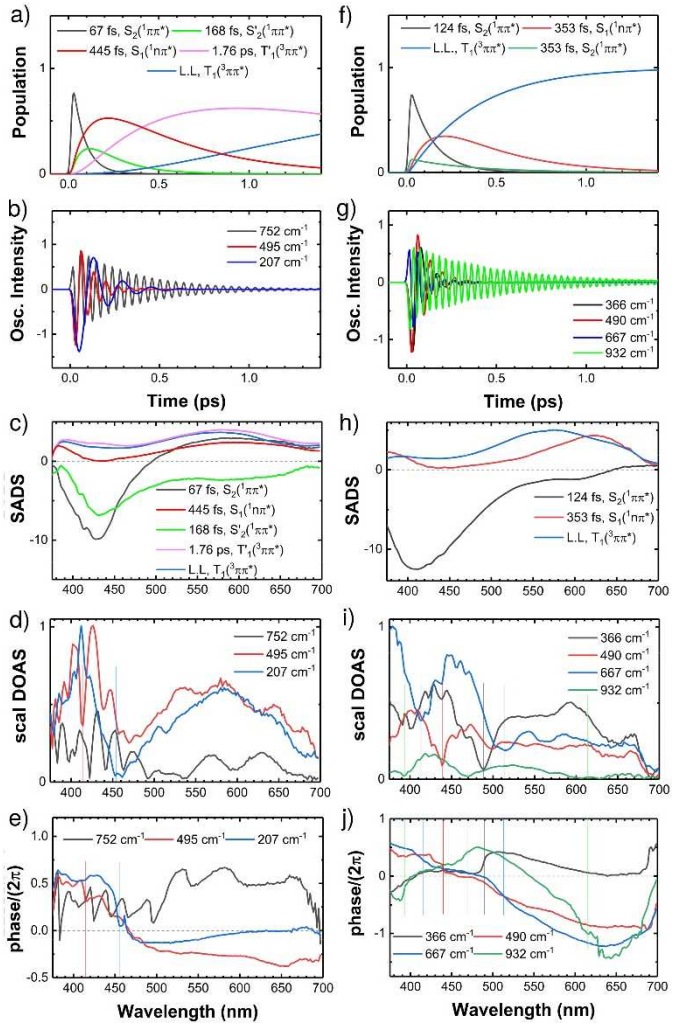

Figure 3-DOAS analysis of 4 TT and 4TU in PBS excited with a 20-fs pulse centered at 330 nm and probed in the visible and overview of the estimated DOAS and phases. a) 4TT and f) 4TU population in each state. b) 4TT and g) 4TU cosine oscillations with frequencies. c) 4TT and h) 4TU estimated SADS. 4TT lifetimes: 67 fs ($S_2(^1\pi\pi^*)$, black), 168 fs ($S_2'(^1\pi\pi^*)$, green), 445 fs ($S_1(^1n\pi^*)$, red), 1.76 ps ($T_1'(^3\pi\pi^*)$, magenta) and long lived ($T_1(^3\pi\pi^*)$, blue). 4TU lifetimes: 124 fs ($S_2(^1\pi\pi^*)$, black curve), 353 fs ($S_1(^1n\pi^*)$, red curve), and long lived ($T_1(^3\pi\pi^*)$, blue curve). d) 4TT and i) 4TU estimated DOAS. e) 4TT and j) 4TU estimated phase profiles of the DOAS. The red and blue dashed vertical lines at 413 nm and 455 nm (panel d and e) are nodes from the modes 495 cm^{-1} and 207 cm^{-1}, respectively. At panel i and j the vertical green lines at 392 nm, 470 nm, and 615 nm are nodes from 932 cm^{-1} mode; the vertical blue lines at 413 nm and at 511 nm are nodes from 667 cm^{-1} mode; the vertical red line at 440 nm is the node from 440 cm^{-1} mode; the vertical red line at 490 nm is the node from 366 cm^{-1} mode.

minimum is associated with bond length rearrangement resulting in values similar to the ones observed at the S_2 minima. In addition, 4TT exhibits a pronounced sulphur out-of-plane bending by 23°. Finally, rather minor geometrical changes occur towards the $T_1(^3\pi\pi^*)$ minimum. Interestingly, 4TT planarizes, whereas 4TU exhibits sulphur and oxygen out-of-plane bending by ca. 10°.

Overall, both systems exhibit comparable bond length deformations but rather different residual geometry changes. While 4TU remains rather planar until it reaches $T_1(^3\pi\pi^*)$, 4TT exhibits out-of-plane deformations already in the singlet manifold.

Now we compare the vibrational modes obtained from the DOAS analyses, Figure 3 (d) and (i), and the calculated normal

modes, Figure 5. By DOAS analyses, the TAS signal is modulated by oscillatory features with frequencies:

a) 207 cm^{-1}, 495 cm^{-1} and 752 cm^{-1} in 4TT

b) 366 cm^{-1}, 490 cm^{-1}, 667 cm^{-1} and 932 cm^{-1} in 4TU.

The 4TT DOAS frequencies are in agreement with the ones obtained by FT study. The 4TU DOAS analysis reproduces and extends our previously reported study[38]. The obtained modes and their damping times are collated in Table 1.

In 4TT we obtained a mode with 495 cm^{-1} frequency showing a strong damping rate of 11 ps^{-1} (~86 fs) with a node at 413 nm in the DOAS curve, accompanied by a phase flip (red vertical line in Figure 3 (d) and (e)). A DOAS curve node accompanied by a corresponding phase flip marks a minimum on the electronic PES[44]. The $S_2(^1\pi\pi^*)$ emission peak at 420 nm (Figure 1 (c)) nicely matches the wavelength of the 413 nm node, strongly suggesting that the 495 cm^{-1} mode is associated with a nuclear wave packet motion around the $S_2(^1\pi\pi^*)$ minimum. Correspondingly, the normal mode analysis (section 5 in the SI) finds a breathing mode along the S_4C_4--N_1H axis coupled to methyl in-plane bending (Figure 5 (b)) with frequency of 493 cm^{-1} which exhibits a large reorganization energy on $S_2(^1\pi\pi^*)$ (Table S7 in SI). The mode exists on $S_1(^1n\pi^*)$ and $T_1(^3\pi\pi^*)$, however, it is not involved in the relaxation. This rationalizes the fast damping time of 86 fs, which is also on the same timescale as the $S_2(^1\pi\pi^*)$ fast relaxation (67 fs). By similar

	$\tau_{S_2(\pi\pi^*)}$ (fs)	$\tau_{S_1(n\pi^*)}$ (fs)	ω_n (cm^{-1})	Nodes (nm)	$1/\gamma_n$ (fs)
4TT	67(S'_2) 168	445	207	455	120
			495	413	86
			752	-	333
4TU	124	353	366	490	67
			490	440	89
			667	413,511	67
			932	392,470,615	476

arguments the 366 cm^{-1} DOAS frequency in 4TU is assigned to a breathing mode along the S_4C_4--N_1H axis (Figure 5 (f)) with calculated frequency of 387 cm^{-1} which is among the modes with the highest reorganization energy below 1000 cm^{-1} (see Table S5 in SI). The mode is relevant only for the relaxation on $S_2(^1\pi\pi^*)$, in agreement with its short damping time of 67 fs.

In 4TT there is a 752 cm^{-1} frequency mode with damping rate of 3.0 ps^{-1} (333 fs) suggesting that the vibration survives the IC and ISC dynamics ($CI_{TT}S_2/S_1$ and ISC_{TT} S_1/T_1 respectively). Our calculations associate the 752 cm^{-1} mode with a breathing mode along the HC_6--N_3H axis with 700 cm^{-1} frequency (Figure 5 (d)) due to its large reorganization energy in $S_2(^1\pi\pi^*)$. The mode is not active in $S_1(^1n\pi^*)$ and $T_1(^3\pi\pi^*)$, which suggests that the low damping rate is a signature of preservation of vibrational coherence upon non-adiabatic decay. We also identified an oxygen in-plane bending coupled to C_5/C_6 contrarywise out-of-plane deformation with 625 cm^{-1} frequency (Figure 5 (c)) and large reorganization energy in $S_1(^1n\pi^*)$. Thus, alternatively, the long coherence lifetime could be explained by the interplay of two modes, the first one activated upon excitation in S_2, the second mode upon IC to S_1.

In 4TU the breathing along the HC_6--N_3H axis and oxygen in-plane bending have calculated frequencies of 675 cm^{-1} and 490 cm^{-1} (Figure 5 (h) and (g)), respectively. It should be noted that the breathing has the highest reorganization energy in $S_2(^1\pi\pi^*)$ whereas the in-plane bending has the highest in $S_1(^1n\pi^*)$ (Table S5). The nearly 200 cm^{-1} splitting of the two modes allows to separate the oscillatory contributions to the spectral dynamics. Accordingly, the DOAS reveal modes with 667 cm^{-1} and 490 cm^{-1} with strong damping rates of 15 ps^{-1} (67 fs) and 11 ps^{-1} (89 fs), respectively. The 667 cm^{-1} mode exhibits nodes at 413 nm and 511 nm (Figure 3 (i) and (j), dashed blue lines), whereas the 490 cm^{-1} mode exhibits one node at 440 nm (Figure 3 (i) and (j), dash red lines). The short damping time of the 667 cm^{-1} mode and the match between the 413 nm node and the wavelengths of the $S_2(^1\pi\pi^*)$ emission indicate that the vibrational coherence does not survive the IC to S_1. The lack of a node at the position of the $S_2(^1\pi\pi^*)$ emission in the 490 cm^{-1} mode corroborates its activation in the $S_1(^1n\pi^*)$ state.

In addition, for 4TT the DOAS analysis reveals a mode with a frequency of 207 cm^{-1} that shows a damping rate of 8.3 ps^{-1} (120 fs) and presents a node at about 455 nm (Figure 3 (d) and (e), dashed blue line). Again, the lack of a node in the DOAS profile at the position of the SE suggests that the associated coherence is not active in $S_2(^1\pi\pi^*)$. Indeed, the normal mode analysis reveals a sulphur and a methyl contrary out-of-plane deformation (Figure 5 (a)) characteristic for 4TT with 218 cm^{-1} frequency. It is the mode with the highest reorganization energy in $S_1(^1n\pi^*)$ as it encompasses the major deformation that leads from the CI to the S_1 minimum. This mode evidences the breaking of planarity of 4TT during its evolution to the triplet manifold.

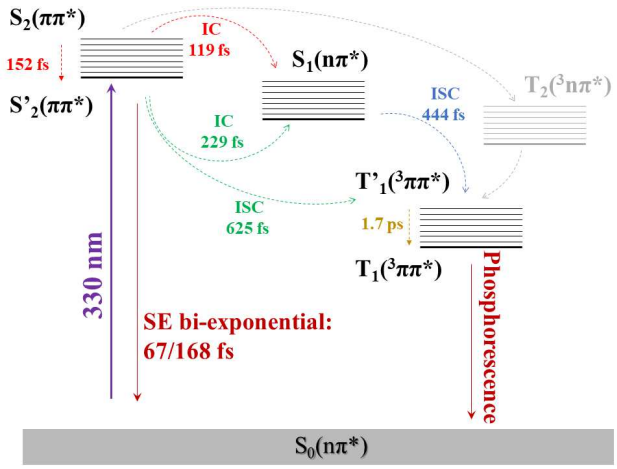

Figure 4- 4TT triplet formation mechanism upon UV photoexcitation (at 330 nm, vertical purple arrow). Two vertical solid red arrows indicate two radioactive processes: first, SE in a biexponential time scale from $S_2(^1\pi\pi^*)$, and later phosphorescence from $T_1(^3\pi\pi^*)$. Dashed arrows indicate the non-radioactive processes. The same colour dashed arrows indicate concurrent processes. Dashed grey arrows show the secondary decay path involving $S_2(^1\pi\pi^*) \rightarrow T_2(^3n\pi^*) \rightarrow T_1(^3\pi\pi^*)$ transitions. Next to the arrows the reciprocal of the rate constant is written.

Finally, the DOAS analysis of 4TU shows a mode with a frequency of 932 cm^{-1} and a comparably long lifetime of 476 fs exhibiting nodes at 392 nm, 470 nm and 615 nm. The first node is in good agreement with the position of the SE from $S_2(^1\pi\pi^*)$, and the second and third nodes match the strongest PA from the $T_1(^3\pi\pi^*)$ (Figure 2). According to the calculations this

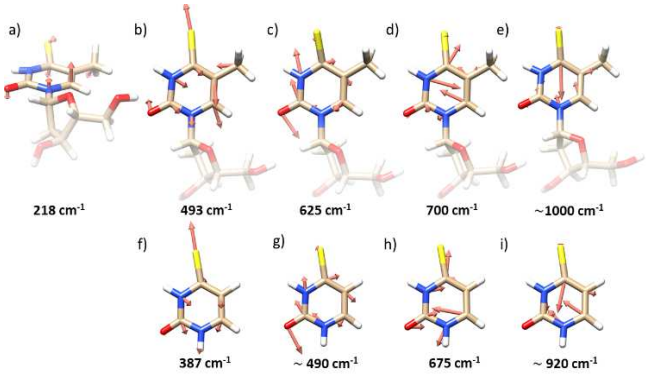

Figure 5- Normal modes of 4TT (a)-e)) and 4-thiouracil (f)-i)) assigned by means of a normal mode analysis (see sec. 5 in the SI) to the frequencies resolved by the DOAS analysis of the experimental data (Figure 3 and Table 1). The depicted modes encompass the major deformations along the relaxation path from the FC point to the T1 minimum. Calculated modes' frequencies are taken from Tables S5 (4TU) and S7 (4TT). The C-S stretching (e) in 4TT is expected to appear around 1000 cm^{-1} and is thus beyond the resolution of the experimental set up.

frequency can be assigned to the C_4-S_4 stretching (Figure 5 (i)) that is active during the relaxational dynamics from the FC to the T_1, thus rationalizing the long coherence lifetime. The stretching exhibits a frequency in the range 902-945 cm^{-1} on the PES of S_2, S_1 and T_1. Also, in 4TT the C_4-S_4 stretching (Figure 5 (e)) is activated upon excitation. It should be noted though that it appears at higher frequencies around 1000 cm^{-1}. This might explain why it is not experimentally detected as it is damped by the high frequency cut-off of our set up.

4 Conclusions

In conclusion, through the combination of: a) transient absorption spectroscopy with very high temporal resolution (sub-30 fs) and broadband probing covering the entire visible spectrum; b) state-of-the-art data analysis which allows to distinguish the contributions of the electronically and vibrationally excited states; and c) computational feedback for state-specific PA/SE fingerprints and the nature of the photoexcited vibrational modes, we capture a detailed molecular movie of the ES dynamics of photoexcited mono-thionated 4-thiouracil and 4-thiothymidine.

Table 1- Summary of 4TT and 4TU DOAS and target analyses findings: time constants $\tau_{S_2(\pi\pi^*)}$ and $\tau_{S_1(\pi\pi^*)}$; ω_n frequency mode; nodes in the DOAS and $1/\gamma_n$ damping time.

We report a clear mismatch between the time scales of the $S_2(^1\pi\pi^*)$ depletion and of the triplet formation in 4TT, which is evidence for the participation of an intermediate state. Our computations identify this state as the singlet S_1 ($^1n\pi^*$) state which acts as the doorway for an efficient ISC to the triplet manifold. This supports the $S_2(^1\pi\pi^*) \rightarrow S_1(^1n\pi^*) \rightarrow T_1(^3\pi\pi^*)$ mechanism (i.e. pathway (i)) as the dominant channel in 4TT, as already established for 4TU. We also find sound evidence for a direct ISC process from $S_2(^1\pi\pi^*)$ (i.e. pathway (ii)) and quantify its role to 10% in 4TT and 40% in 4TU.

Despite sharing a similar molecular structure of the base, differing solely in the substitution of a hydrogen by a methyl group, and comparable decay mechanisms, the geometrical deformations in 4TT and 4TU along the IC and ISC pathways are surprisingly dissimilar, characterized by conservation of planarity in 4TU and its partial rupture in 4TT. The DOAS and normal mode analysis allow us to identify the modes below 1000 cm^{-1} with appreciable reorganisation energy that drive the IC and ISC processes. In particular, we report a 4TT specific mode with a 207 cm^{-1} frequency, involving methyl and sulphur out-of-plane deformations in support of the "breaking of planarity" IC pathway undergone by 4TT.

Author Contributions

R.B.V., L.G and C.M. built the experimental setup, D.C.T.F performed the measurements, I.H.M.vS. implemented the DOAS and target analysis methodology, I.C. and A.N. performed the theoretical calculations, G.C., M.G. and A.M.dP. conceived the idea and supervised the project, all the authors discussed the results and data analysis, D.C.T.F, I.H.M.v.S, R.B.V., I.C., A.N. and A.M.dP. wrote the manuscript with inputs from all the authors.

Conflicts of interest

There are no conflicts to declare.

Acknowledgements

D.C.T.F. and A.M.d.P. acknowledge financial support from the funding agencies Fapemig, CNPq, and CAPES. I.H.M.v.S. and G.C. acknowledge funding from the European Union's Horizon 2020 research and innovation programme under grant agreement no 654148 Laserlab-Europe.

Notes and references

1 B. Ashwood, M. Pollum and C. E. Crespo-Hernández, *Photochem. Photobiol.*, 2019, **95**, 33–58.

2 S. Arslancan, L. Martínez-Fernández and I. Corral, *Molecules*, 2017, **22**, 998.

3 J. M. L. Pecourt, J. Peon and B. Kohler, *J. Am. Chem. Soc.*, 2001, **123**, 10370–10378.

4 A. Nenov, I. Conti, R. Borrego-Varillas, G. Cerullo and M. Garavelli, *Chem. Phys.*, 2018, **515**, 643–653.

5 C. T. Middleton, K. de La Harpe, C. Su, Y. K. Law, C. E. Crespo-Hernández and B. Kohler, *Annu. Rev. Phys. Chem.*, 2009, **60**, 217–239.

6 G. Cerullo and M. Garavelli, *Proc. Natl. Acad. Sci. U. S. A.*, 2020, **117**, 26553–26555.

7 V. I. Prokhorenko, A. Picchiotti, M. Pola, A. G. Dijkstra and R. J. D. Miller, *J. Phys. Chem. Lett.*, 2016, **7**, 4445–4450.

8 R. Borrego-Varillas, A. Nenov, P. Kabaciński, I. Conti, L. Ganzer, A. Oriana, V. K. Jaiswal, I. Delfino, O. Weingart, C.

Manzoni, I. Rivalta, M. Garaveli and G. Cerullo, *Nat. Commun.*, 2021, **12**, 7285.
9 M. Pollum, M. Lam, S. Jockusch and C. E. Crespo-Hernández, *ChemMedChem*, 2018, **13**, 1044–1050.
10 M. Pollum, S. Jockusch and C. E. Crespo-Hernández, *Phys. Chem. Chem. Phys.*, 2015, **17**, 27851–27861.
11 M. Pollum, L. A. Ortiz-Rodriguez, S. Jockusch and C. E. Crespo-hern, *Photochem. Photobiol.*, 2016, 286–292.
12 S. Mai, P. Marquetand and L. González, *J. Phys. Chem. A*, 2015, **119**, 9524–9533.
13 S. Mai, M. Pollum, L. Martínez-Fernández, N. Dunn, P. Marquetand, I. Corral, C. E. Crespo-Hernández and L. González, *Nat. Commun.*, 2016, **7**, 13077.
14 S. Mai, P. Marquetand and L. González, *J. Phys. Chem. Lett.*, 2016, **7**, 1978–1983.
15 B. Ashwood, S. Jockusch and C. E. Crespo-Hernández, *Molecules*, 2017, **22**, 379.
16 M. Pollum, S. Jockusch and C. E. Crespo-hernández, *J. Am. Chem. Soc.*, 2014, **136**, 17930–17933.
17 C. Reichardt, C. Guo and C. E. Crespo-Hernández, *J. Phys. Chem. B*, 2011, **115**, 3263–3270.
18 C. Reichardt and C. E. Crespo-Hernaíndez, *J. Phys. Chem. Lett.*, 2010, **1**, 2239–2243.
19 O. Reelfs, P. Karran and A. R. Young, *Photochem. Photobiol. Sci.*, 2012, **11**, 148–154.
20 A. Massey, Y. Z. Xu and P. Karran, *Curr. Biol.*, 2001, **11**, 1142–1146.
21 A. Favre, G. Moreno, M. O. Blondel, J. Kliber, F. Vinzens and C. Salet, *Biochem. Biophys. Res. Commun.*, 1986, **141**, 847–854.
22 M. Harris, H. Cote, C. Ochoa, C. Allavena, E. Negredo, P. Cahn, C. Zala and F. Raffi, *J. Acquir. Immune Defic. Syndr.*, 2009, **50**, 339–340.
23 K. M. Meisenheimer and T. H. Koch, *Crit. Rev. Biochem. Mol. Biol.*, 1997, **32**, 101–140.
24 M. Pollum and C. E. Crespo-Hernández, *J. Chem. Phys.*, 2014, **140**, 071101.
25 H. Yu, J. A. Sanchez-Rodriguez, M. Pollum, C. E. Crespo-Hernández, S. Mai, P. Marquetand, L. González and S. Ullrich, *Phys. Chem. Chem. Phys.*, 2016, **18**, 20168–20176.
26 J. A. Sánchez-Rodríguez, A. Mohamadzade, S. Mai, B. Ashwood, M. Pollum, P. Marquetand, L. González, C. E. Crespo-Hernández and S. Ullrich, *Phys. Chem. Chem. Phys.*, 2017, **19**, 19756–19766.
27 X. Zou, X. Dai, K. Liu, H. Zhao, D. Song and H. Su, *J. Phys. Chem. B*, 2014, **118**, 5864–5872.
28 Y. Nam, D. Keefer, A. Nenov, I. Conti, F. Aleotti, F. Segatta, J. Y. Lee, M. Garavelli and S. Mukamel, *J. Phys. Chem. Lett.*, 2021, **12**, 12300–12309.
29 D. C. Teles-Ferreira, C. Manzoni, L. Martínez-Fernández, G. Cerullo, A. M. de Paula and R. Borrego-Varillas, *Molecules*, 2022, **27**, 1–10.
30 H. Yu, J. A. Sanchez-Rodriguez, M. Pollum, C. E. Crespo-Hernández, S. Mai, P. Marquetand, L. González and S. Ullrich, *J. Phys. Chem. B*, 2016, **5**, 2239–2243.
31 M. Ruckenbauer, S. Mai, P. Marquetand and L. González, *J. Chem. Phys.*, 2016, **144**, 074303.
32 Y. Huang, F. Xu, L. Ganzer, F. V. A. Camargo, T. Nagahara, J. Teyssandier, H. Van Gorp, K. Basse, L. A. Straasø, V. Nagyte, C. Casiraghi, M. R. Hansen, S. De Feyter, D. Yan, K. Müllen, X. Feng, G. Cerullo and Y. Mai, *J. Am. Chem. Soc.*, 2018, jacs.8b06028.
33 J. Jiang, T. S. Zhang, J. D. Xue, X. Zheng, G. Cui and W. H. Fang, *J. Chem. Phys.*, 2015, **143**, 11B605_1.
34 B.-B. Xie, Q. Wang, W.-W. Guo and G. Cui, *Phys. Chem. Chem. Phys.*, 2017, **19**, 7689–7698.
35 L. Martinez-Fernandez, T. Fahleson, P. Norman, F. Santoro, S. Coriani and R. Improta, *Photochem. Photobiol. Sci.*, 2017, **16**, 1415–1423.
36 Throughout this work 4TU refers to the bare nucleic acid whereas 4TT refers to the nucleoside only in the experimental results.
37 D. C. Teles-Ferreira, I. Conti, R. Borrego-Varillas, A. Nenov, I. H. M. Van Stokkum, L. Ganzer, C. Manzoni, A. M. de Paula, G. Cerullo and M. Garavelli, *Chem. - A Eur. J.*, 2020, **26**, 336–343.
38 R. Borrego-varillas, D. C. Teles-ferreira, A. Nenov, I. Conti, L. Ganzer, C. Manzoni, M. Garavelli, A. M. de Paula and G. Cerullo, *J. Am. Chem. Soc*, 2018, **140**, 16087−16093.
39 G. Cui and W. Thiel, *J. Phys. Chem. Lett.*, 2014, **5**, 2682–2687.
40 Y. Harada, C. Okabe, T. Kobayashi, T. Suzuki, T. Ichimura, N. Nishi and Y. Z. Xu, *J. Phys. Chem. Lett.*, 2010, **1**, 480–484.
41 Y. Harada, T. Suzuki, T. Ichimura and Y. Z. Xu, *J. Phys. Chem. B*, 2007, **111**, 5518–5524.
42 L. Martínez-Fernández, G. Granucci, M. Pollum, C. E. Crespo-Hernández, M. Persico and I. Corral, *Chem. - A Eur. J.*, 2017, **23**, 2619–2627.
43 I. H. M. van Stokkum, M. Kloz, D. Polli, D. Viola, J. Weißenborn, E. Peerbooms, G. Cerullo and J. T. M. Kennis, *J. Chem. Phys.*, 2021, **155**, 114113.
44 I. H. M. Van Stokkum, C. C. Jumper, J. J. Snellenburg, G. D. Scholes, R. Van Grondelle and P. Malý, *J. Chem. Phys.*, 2016, **145**, 174201-1-174201–13.
45 R. Borrego-Varillas, L. Ganzer, G. Cerullo and C. Manzoni, *Appl. Sci.*, 2018, **8**, 989.
46 R. B. Varillas, A. Candeo, D. Viola, M. Garavelli, S. De Silvestri, G. Cerullo, C. Manzoni, S. De Silvestri, G. Cerullo, C. Manzoni, S. De Silvestri, G. Cerullo and C. Manzoni, *Opt. Lett.*, 2014, **39**, 3849–3852.
47 R. Borreco-Varillas, A. Oriana, F. Branchi, de S. Silvestri, G. Cerullo and C. Manzoni, *J. Opt. Soc. Am. B*, 2015, **32**, 1851–1855.
48 D. A. Case, T. A. Darden, T. E. Cheatham, III, C. L. Simmerling, J. Wang, R. E. Duke, R. Luo, R. C. Walker, W. Zhang, K. M. Merz, B. Roberts, S. Hayik, A. Roitberg, G. Seabra, J. Swails, A. W. Götz, I. Kolossváry, K. F. Wong, F. Paesani, J. Vanicek, R. M. J. Wolf and P. A. Kollman, *AMBER 12 University of California*, San Francisco, 2012.
49 R. Salomon-Ferrer, D. A. Case and R. C. Walker, *Wiley Interdiscip. Rev. Comput. Mol. Sci.*, 2013, **3**, 198–210.
50 W. L. Jorgensen, J. Chandrasekhar, J. D. Madura, R. W. Impey and M. L. Klein, *J. Chem. Phys.*, 1983, **79**, 926–935.
51 J. P. Ryckaert, G. Ciccotti and H. J. C. Berendsen, *J. Comput. Phys.*, 1977, **23**, 327–341.
52 S. Miyamoto and P. A. Kollman, *J. Am. Chem. Soc.*, 1992,

114, 3668–3674.
53 P.-O. Widmark, P.-Å. Malmqvist and B. O. Roos, *Theor. Chem. Acc.*, 1990, **77**, 291–306.
54 T. Shiozaki, W. Gyroffy, P. Celani and H. J. Werner, *J. Chem. Phys.*, 2011, **135**, 97–100.
55 G. Ghigo, B. O. Roos and P. Å. Malmqvist, *Chem. Phys. Lett.*, 2004, **396**, 142–149.
56 N. Forsberg and P. Å. Malmqvist, *Chem. Phys. Lett.*, 1997, **274**, 196–204.
57 I. Fdez. Galván, M. Vacher, A. Alavi, C. Angeli, F. Aquilante, J. Autschbach, J. J. Bao, S. I. Bokarev, N. A. Bogdanov, R. K. Carlson, L. F. Chibotaru, J. Creutzberg, N. Dattani, M. G. Delcey, S. S. Dong, A. Dreuw, L. Freitag, L. M. Frutos, L. Gagliardi, F. Gendron, A. Giussani, L. González, G. Grell, M. Guo, C. E. Hoyer, M. Johansson, S. Keller, S. Knecht, G. Kovačević, E. Källman, G. Li Manni, M. Lundberg, Y. Ma, S. Mai, J. P. Malhado, P. Å. Malmqvist, P. Marquetand, S. A. Mewes, J. Norell, M. Olivucci, M. Oppel, Q. M. Phung, K. Pierloot, F. Plasser, M. Reiher, A. M. Sand, I. Schapiro, P. Sharma, C. J. Stein, L. K. Sørensen, D. G. Truhlar, M. Ugandi, L. Ungur, A. Valentini, S. Vancoillie, V. Veryazov, O. Weser, T. A. Wesołowski, P. O. Widmark, S. Wouters, A. Zech, J. P. Zobel and R. Lindh, *J. Chem. Theory Comput.*, 2019, **15**, 5925–5964.
58 F. Aquilante, J. Autschbach, A. Baiardi, S. Battaglia, V. A. Borin, L. F. Chibotaru, I. Conti, L. De Vico, M. Delcey, I. F. Galván, N. Ferré, L. Freitag, M. Garavelli, X. Gong, S. Knecht, E. D. Larsson, R. Lindh, M. Lundberg, P. Å. Malmqvist, A. Nenov, J. Norell, M. Odelius, M. Olivucci, T. B. Pedersen, L. Pedraza-González, Q. M. Phung, K. Pierloot, M. Reiher, I. Schapiro, J. Segarra-Martí, F. Segatta, L. Seijo, S. Sen, D. C. Sergentu, C. J. Stein, L. Ungur, M. Vacher, A. Valentini and V. Veryazov, *J. Chem. Phys.*, 2020, **152**, 5925–5964.
59 O. Weingart, A. Nenov, P. Altoè, I. Rivalta, J. Segarra-Martí, I. Dokukina and M. Garavelli, *J. Mol. Model.*, 2018, **24**, 1–30.
60 *The exploration of the PES at XMS-CASPT2 level, which relies on an averaged Fock operator, deteriorates when state-averaging is performed over a large number of states, due to that we opted in favour of MS-CASPT2 for the computation of the PA features*, .
61 S. Bai and M. Barbatti, *Phys. Chem. Chem. Phys.*, 2017, **19**, 12674–12682.
62 J. Cao and D. C. Chen, *Phys. Chem. Chem. Phys.*, 2020, **22**, 10924–10933.